Consiglio Nazionale delle Ricerche

ISTITUTO DI ELABORAZIONE DELLA INFORMAZIONE

PISA

An Acoustic Pyrometer System for Tomographic Thermal Imaging in Power Plant Boilers

M.Bramanti, A.Gray, S.Pasini,
E.A.Salerno, A.Tonazzini

Nota Interna B4-21

luglio 1994

An Acoustic Pyrometer System for Tomographic Thermal Imaging in Power Plant Boilers

Abstract: The paper presents an acoustic pyrometry method for the reconstruction of temperature maps inside power plant boilers. It is based on measuring times-of-flight of acoustic waves along a number of straight paths in a cross-section of the boiler; via an integral relationship, these times depend on the temperature of the gaseous medium along the paths. On this basis, 2D temperature maps can be reconstructed using suitable inversion techniques. The structure of a particular system for the measurement of the times-of-flight is described and two classes of reconstruction algorithms are presented. The algorithms proposed have been applied to both simulated and experimental data measured in power plants of the Italian National Electricity Board (ENEL). The results obtained appear fairly satisfactory, considering the small data sets that it was possible to acquire in the tested boilers.

1. Introduction

The availability of maps of the internal temperatures of a boiler is very important in the design of low NO_X combustion systems, as the presence of hot spots increases NO_X generation. However, the mapping of an industrial boiler with a conventional probe is not an easy task and it is very difficult to obtain a significant set of data.

Temperature maps can also be obtained using optical technologies, but these technologies are complex and, moreover, cannot be used with all

kinds of fuel. For example, in coal-fired power plant boilers, optical instruments cannot be used.

Fortunately, acoustic pyrometer does not impose limits of this type and measurements can be performed using a relatively simple instrumentation. The acoustic pyrometer presented in this paper can function as a stand-alone system in boilers whose power does not exceed 80-100 MWe; for larger boilers, the measurements must be taken by skilled operators.

An acoustic pyrometer system measures the *times-of-flight* (TOF) of acoustic waves between several couples of points placed on the walls of the boiler. By using these data and suitable reconstruction algorithms, the temperature map can be reconstructed for the entire probed plane.

In this paper, after a brief review of acoustic pyrometry theory, the application of a number of image reconstruction techniques to the particular problem being examined is analyzed. Successively, the structure of a particular acoustic pyrometer, installed at ENEL's Santa Gilla (Sardinia) power plant, is described and the results obtained by applying the considered reconstruction techniques to the measured data are presented.

2. Principles of acoustic pyrometry

The measurement of acoustic parameters to determine certain thermodynamic conditions of a gaseous medium was first proposed in 1873 and has recently been developed by several authors (see [1, 2]). In particular, if the TOF of an acoustic signal travelling between two fixed points is known, then we can estimate the velocity of sound in the medium, which is related to its temperature.

As is known, the velocity of sound in a gaseous medium at an absolute temperature T is given by:

$$v_s = \sqrt{\frac{dP}{d\rho}} \qquad (2.1)$$

where P is the gas pressure and ρ is its mass-density. If the gas is ideal, with a known temperature and chemical composition, and if we presume that we have no heat transfer associated with the acoustic wave propagation, (2.1) becomes:

$$v_s = \sqrt{\frac{\gamma RT}{m}} = z\sqrt{T} \qquad (2.2)$$

where γ is the ratio between the specific heats at constant pressure and volume of the gas, R is the gas constant, and m is the molecular weight of the gas.

Let us now suppose that the gas is contained in a power plant boiler, of which we consider a particular cross-section with an associated two-dimensional coordinate system x-y. If f(x,y) is the slowness function, defined as the reciprocal of v_s, the TOF of a sonic signal over a path p is given by:

$$\tau = \int_p f(x(l),\ y(l))\ dl \qquad (2.3)$$

where l is a suitable curvilinear abscissa chosen on p. On the basis of TOF measurements and of the knowledge of the path lengths, we can thus evaluate the mean sound slowness over each path, and give an estimate of the mean temperature in the boiler. If we have sufficient data available, we can also apply reconstruction techniques to estimate function f(x,y) and to map the behaviour of the temperature T(x,y) using relation (2.2). This possibility will be discussed in Section 3.

Unfortunately, there are various sources of uncertainty that reduce the reliability of the reconstruction. Apart from inaccuracies in the evaluation of the physical parameters involved in (2.2), in practice each TOF will be the result of a measurement procedure and will be affected by a measurement error. Furthermore the sound paths in the boiler cannot be known accurately as, by Fermat's principle, they depend upon the sound velocity distribution in the medium, and this is unknown. The only data that we can obtain with true accuracy are the coordinates of the ends of each sound path. Bending in these paths, which is due to the nonuniformity of the velocity field, can be treated using nonlinear image reconstruction techniques (see, for example, [3]). However, in our case, it has been evaluated that this error source can be ignored providing the path does not form large angles with the direction of the temperature gradient in those regions where its magnitude assumes large values (typically in proximity of the boiler walls). For this reason, in the following we will consider the paths to be rectilinear. If necessary, this error can be corrected iteratively. An analysis of the various error sources is reported in [2].

3. The reconstruction problem

As previously explained, an estimation of the temperature map requires a reconstruction of the slowness function f(x,y) over the cross-section D of the boiler probed by the sonic signal. The N_d TOF measurements available are related to the unknown function via the following line-integrals:

$$g_k = \int_{l_k} f(x,y)\ dl_k + n_k, \quad k = 1, \ldots, N_d \tag{3.1}$$

where, for any k, l_k is a straight path contained in D (see Figure 1) and n_k is the system noise, which is the sum of the various error terms affecting the measurement.

Our problem consists in the estimation of function f(x,y), given the data vector **g** and the integration paths, and can be seen as a particular case of the more general problem of image reconstruction from projections, widely studied in medical imaging and in several other application fields [1, 3-6]. In our case, as the data set is normally very small, this problem can be seen as image reconstruction from *sparse* samples of *sparse* projections.

3.1 Standard regularization approaches

The reconstruction of images is an inverse problem and is generally recognizable as being ill-posed in the sense of Hadamard [7], in that the existence, uniqueness and stability of the solution cannot be guaranteed. In this case, the ill-posedness of the problem is mainly due to the non-uniqueness and instability of the solution. Indeed, since the solution space is infinite-dimensional while the number of data is finite, there will be an infinite set of functions yielding the same data. Moreover, the presence of the noise on the data can result in very poor solutions even if the dimensionality of the solution space is restricted to that of the data space.

A possible step towards the computation of a unique solution might be to expand f(x,y) over a finite set of continuous basis functions $h_m(x,y)$, namely to *parametrize* the solution:

$$f(x,y) = \sum_{m=1}^{N_p} a_m \, h_m(x,y) \qquad (3.2)$$

where a_m are the *parameters* of the model. By (3.2), we can re-write Eq. (3.1) as:

$$g_k = \sum_{m=1}^{N_p} a_m \int_{l_k} h_m(x,y)\ dl + n_k, \quad k=1,...,N_d \qquad (3.3).$$

In this discrete formulation, our reconstruction problem becomes the resolution of the linear system (3.3), where the N_p parameters a_m are now the unknowns to be determined. In this case, the noise can also include a third term resulting from the possibly inadequate parametrization.

Let us write Eq. (3.3) in vector form:

$$\mathbf{g} = H\mathbf{a} + \mathbf{n} \qquad (3.4),$$

where H is an $N_d \times N_p$ matrix. If we ignore the noise, least squares or pseudo-inverse solutions for (3.4) exist; however, these solutions are in general highly noise sensitive, due to the typically ill-conditioned nature of this kind of problem [8].

The basic strategy for selecting a solution that is unique and robust against noise (i.e. *regularizing* the problem), is to restrict the class of feasible solutions by imposing constraints that exploit any additional information concerning the properties of the solution and/or the noise. The most popular approach to regularization consists in reformulating the problem as a well-posed, well-conditioned, constrained optimization problem [8, 9]. In practice, a *cost functional*, or *stabilizer*, representing some measure of *regularity* in the solution, is optimized on the set of images satisfying certain requirements, in the form of constraint maps.

As prior information, we assume that the variance σ^2 of the system noise, assumed to be Gaussian, is known. This knowledge leads to the

formulation of a constraint relation on the vector **a** to be estimated. If C(**a**) is the cost functional chosen, the problem may be formulated as:

$$\text{minimize} \quad C(\mathbf{a}) \tag{3.5 a}$$

$$\text{subject to} \quad \|\mathbf{g} - H\mathbf{a}\|^2 \leq N_d \sigma^2 \tag{3.5 b}.$$

The constraint (3.5 b) defines the set of feasible solutions as the set of vectors **a** such that the *residual*, $\|\mathbf{g} - H\mathbf{a}\|^2$, is no greater than $N_d \sigma^2$ [6]. If C(**a**) is a convex functional, then problem (3.5) has a unique solution, which can be computed as the solution of an equivalent unconstrained optimization problem:

$$\min_{\mathbf{a}} \|\mathbf{g} - H\mathbf{a}\|^2 + \lambda C(\mathbf{a}) \tag{3.6}$$

for a particular non-negative value of the *regularization parameter* λ [7, 10]. Instead of calculating the exact value of λ, we consider it simply as a weight that determines a compromise between the regularity of the solution and its fit to the data. As a particular solution to (3.6) in the case $N_d > N_p$ we have, for $\lambda = 0$, the unconstrained least squares solution; in the case $N_d < N_p$, if $C(\mathbf{a}) = \|\mathbf{a}\|^2$ and we let λ go to 0, we find the pseudo-inverse solution [11].

We considered the stabilizer to be a quadratic functional of the form:

$$C(\mathbf{a}) = \|B\mathbf{a}\|^2 \tag{3.7}.$$

In this case, if matrix $(H^TH + \lambda B^TB)$ is nonsingular, solving (3.6) results in [8, 11]:

$$\hat{\mathbf{a}} = \left(H^TH + \lambda B^TB\right)^{-1} H^T \mathbf{g} \tag{3.8}.$$

Let us observe that H^TH and B^TB are positive semi-definite matrices and λ is a positive parameter; thus a sufficient condition for $(H^TH + \lambda B^TB)$ to be nonsingular is that the intersection of the null spaces of H and B contains only the null vector.

In our experiments, we chose the form of B so that the stabilizer (3.7) represents an energy measure for the gradient of function f(x,y). Adopting this stabilizer, the solution to (3.6) for a nonzero value of λ will be forced to be slowly varying. This *smoothness* constraint is normally assumed in image reconstruction and, for the particular case of sonic pyrometry considered here, has an evident physical meaning.

Matrices H and B assume different forms depending on the particular parametrization chosen. In our case, we adopted either a 2D Fourier parametrization [1, 2], or a uniform sampling.

With reference to Fourier parametrization, let us suppose, as shown in Figure 1, that the support D of f(x,y) is rectangular, with dimensions L_x and L_y. If we consider f(x,y) on D as part of a function that is symmetric with respect to the x and y axes and, furthermore, periodic with periods $2L_x$ and $2L_y$ in x and y directions, respectively, then we can expand it as a double Fourier series with only cosinusoidal terms:

$$f(x,y) = \sum_{i=0}^{\infty} \sum_{j=0}^{\infty} A_{ij} \cos(i\pi u) \cos(j\pi v) \qquad (3.9).$$

where

$$u = \frac{x}{L_x}, \qquad v = \frac{y}{L_y}$$

The integrals (3.1) become:

$$g_k = \sum_{i=0}^{\infty} \sum_{j=0}^{\infty} A_{ij}\, h_{k,ij} + n_k, \quad k = 1, \ldots, N_d \tag{3.10}$$

with

$$h_{k,ij} = \int_{l_k} \cos(i\pi u)\ \cos(j\pi v)\ dl_k\ .$$

By physical considerations on f(x,y), we can limit the maximum orders for i and j, and obtain a finite parametrization for f, with N_p parameters. If we order the double-indexed coefficients A_{ij} to form a single indexed vector **a** ($a_m = A_{i_m\, j_m}$, $m = 1, \ldots, N_p$), Eq. (3.9) will assume the form of the linear system in (3.4). In [1] and [2], this system is solved using an unconstrained least-squares approach. However, we have observed [12, 13] that the problem is highly ill-conditioned, with a condition number highly dependent on the number and positions of the integration paths. In particular, any symmetry between different paths should, if possible, be avoided to prevent nearly equal rows and/or columns in matrix H. The condition number decreases as the number of integration paths increases; furthermore the integration paths should cover support region D as uniformly as possible.

The appropriate form of B to obtain the gradient stabilizer for the case of Fourier parametrization has been calculated through integration of the function $|\nabla f|^2$, expressed by way of (3.9), over the image support D. Ordering the indices as shown above, we obtain a pure quadratic form of the coefficients, characterized by a diagonal N_p-order matrix, whose m-th element is:

$$b_{mm} = \begin{cases} \frac{\pi}{\sqrt{2}} \sqrt{i_m^2 \frac{L_y}{L_x}} & \text{if } j_m = 0 \\ \frac{\pi}{\sqrt{2}} \sqrt{j_m^2 \frac{L_x}{L_y}} & \text{if } i_m = 0 \\ \frac{\pi}{2} \sqrt{i_m^2 \frac{L_y}{L_x} + j_m^2 \frac{L_x}{L_y}} & \text{if } i_m \neq 0 \text{ and } j_m \neq 0 \end{cases} \qquad (3.11)$$

It can easily be observed that for this choice the solution in (3.8) is defined, since the square matrix $(H^TH + \lambda B^TB)$ is nonsingular. Indeed, the null space of matrix H represents all the functions with null integrals over the selected paths, while the null space of B represents all the constant functions over D. Note that the vectors representing constant functions do not belong to the null space of H, except for the null function; therefore the intersection of the null spaces of H and B contains only the null vector.

Uniform sampling is a rather obvious way to represent a continuous function through a finite set of parameters. This is normally done in algebraic methods for tomographic reconstruction, especially in medical applications. This parametrization consists in assuming that function f(x,y) is constant over each pixel of an M×N rectangular grid. Following this approach, the basis functions in (3.2) assume the form (see Figure 2):

$$h_m(x,y) = \begin{cases} 1 & \text{if } (x,y) \in \Omega_m \\ 0 & \text{otherwise} \end{cases}, \quad m = 1, \ldots, M \cdot N \qquad (3.12)$$

Adopting the notation previously introduced, we have $N_p = M \cdot N$ and f(x,y) is represented by the vector $\mathbf{f} = \{f_i, i = 1, \ldots, N_p\}$ of samples ordered as shown in Figure 2. In this case, (3.1) becomes:

$$g_k = \sum_{m=1}^{N_p} f_m \cdot d_{mk} + n_k, \quad k = 1, \ldots, N_d \tag{3.13}$$

where d_{mk} is the length of the intersection of Ω_m with the k-th integration path.

Note that in our application this approach normally leads to the condition $N_p > N_d$, and a unique least-squares solution does not exist. Even the pseudo-inverse solution can be very unsatisfactory if $N_p >> N_d$.

Using the sampling parametrization we have:

$$C(f) = \|A_h f\|^2 + \|A_v f\|^2 \tag{3.14}$$

with:

$$A_h = \begin{bmatrix} [I_{M\times M}] & [-I_{M\times M}] & [0_{M\times M}] & \cdots & [0_{M\times M}] & [0_{M\times M}] \\ [0_{M\times M}] & [I_{M\times M}] & [-I_{M\times M}] & \cdots & [0_{M\times M}] & [0_{M\times M}] \\ \cdots & \cdots & \cdots & \cdots & \cdots & \cdots \\ [0_{M\times M}] & [0_{M\times M}] & [0_{M\times M}] & \cdots & [I_{M\times M}] & [-I_{M\times M}] \end{bmatrix} \tag{3.15 a}$$

and

$$A_v = \begin{bmatrix} [A_{(M-1)\times M}] & [0_{(M-1)\times M}] & \cdots & [0_{(M-1)\times M}] \\ [0_{(M-1)\times M}] & [A_{(M-1)\times M}] & \cdots & [0_{(M-1)\times M}] \\ \cdots & \cdots & \cdots & \cdots \\ [0_{(M-1)\times M}] & [0_{(M-1)\times M}] & \cdots & [A_{(M-1)\times M}] \end{bmatrix} \tag{3.15 b}$$

where A_h is a block-band matrix of size $[M\cdot(N-1)]\times[M\cdot N]$ and A_v is a block-diagonal matrix of size $[(M-1)N]\times[MN]$. $I_{M\times M}$ is the identity matrix of size M, $0_{K\times L}$ is the null matrix of size K×L and the band matrix A, of size (M-1)×M is:

$$A_{(M-1)\times M} = \begin{bmatrix} 1 & -1 & 0 & \dots & 0 & 0 \\ 0 & 1 & -1 & \dots & 0 & 0 \\ \dots & \dots & \dots & \dots & \dots & \dots \\ 0 & 0 & 0 & \dots & 1 & -1 \end{bmatrix} \qquad (3.15\ c)$$

As can be easily seen, $A_h f$ and $A_v f$ are approximations of the horizontal and the vertical components of $\nabla f(x,y)$ respectively.

Problem (3.6) has thus a solution in the form (3.8), given by:

$$\hat{f} = \left[H^T H + \lambda \left(A_h^T A_h + A_v^T A_v \right) \right]^{-1} H^T g \qquad (3.16)$$

Again, in this case, the bracketed $N_p \times N_p$ matrix is nonsingular, in that the null spaces of H, A_h and A_v only intersect in the null vector.

3.2 A particular successive-steps procedure

The reconstruction procedures described above present some drawbacks, which will be discussed in Section 5. To partially overcome these drawbacks, a particular reconstruction technique has been developed. This technique is based on two steps: the reconstruction of the temperature function along each path, followed by a suitable interpolation procedure to obtain the temperature map over the whole region D. This approach gave noise-robust results in the cases experimented. We assume that the data set contains the times-of-flight, as defined in Section 2, and the temperature values at the ends of the integration paths:

$$\{ g_k,\ T_{0k} = T(x_{0k},\ y_{0k}),\ T_{1k} = T(x_{1k},\ y_{1k}) \},\qquad k = 1, \dots, N_d \qquad (3.17)$$

where (x_{0k}, y_{0k}) and (x_{1k}, y_{1k}) are the coordinates of the ends of the k-th path on the domain D (see again Figure 1). The mean velocity of sound over the k-th path will be:

$$v_{mk} = \frac{L_k}{g_k} \tag{3.18}$$

where L_k is the length of path l_k. Using the same notation as in Section 2, let us now assume as a first approximation of mean temperature over the path the following quantity:

$$T_{mk} = \frac{v_{mk}^2}{z^2} \tag{3.19}$$

Knowing T_{0k}, T_{1k} and T_{mk}, we can compute a three-parameter approximation $\hat{T}_k(x,y)$ of the temperature function along the k-th integration path. On the basis of this approximation, we can calculate a new estimate of the mean velocity by the relation:

$$v'_{mk} = \frac{1}{L_k} \int_0^{L_k} z \sqrt{\hat{T}_k(x,y)}\, dl_k \tag{3.20}$$

and consequently a new value for the mean temperature, T'_{mk}, and a new approximation function, $\hat{T}'_k(x,y)$. A new value v''_{mk} can then be calculated through (3.20): the iterative process stops when the difference between the latest computed mean value and the previous one is below a preassigned threshold value. The procedure described above allows us to obtain a temperature profile for each integration path; already available interpolation procedures can then be applied to predict the value of the temperature over the entire region D [14-16].

In a first implementation of this method, the temperature profile has been chosen as a parabola:

$$\hat{T}_k(x,y) = A_k s_k^2 + B_k s_k + C_k \tag{3.21}$$

where s_k is the curvilinear abscissa along the k-th integration path. After trivial manipulations, we have:

$$A_k = \frac{6}{L_k^2}\left(\frac{T_{0k} + T_{1k}}{2} - T_{mk}\right)$$

$$B_k = \frac{6}{L_k^2}\left(T_{mk} - \frac{T_{1k} + 2T_{0k}}{3}\right) \qquad (3.22)$$

$$C_k = T_{0k}$$

The reconstruction of the temperature values over the entire domain has been obtained using the estimated values along the propagation paths to calculate the temperature value on a grid with a suitable size. The value at each node of the grid is estimated by weighting, in accordance with an inverse square distance law, the values that are inside a circle of radius *R* (searching radius) centered on the node itself. The thus reconstructed function can be successively smoothed to avoid possible "ridges" in the final maps.

4. The measurement system [17-20]

In Figure 3, a logic diagram of the system (PYRA) used for TOF measurements, relative to a pair of T/R transducers, is shown. This system basically consists of two acoustic transducers with matching exponential horns, a signal generation system, which supplies a coherent sinusoidal pulse sequence, and a receiver for suitable signal conditioning and TOF estimation. The operation of the entire system is governed by a microprocessor-based controller.

The signal generator sythesizes a coherent sinusoidal pulse sequence with a 1800 Hz carrier, pulse duration τ = 6.6 ms and PRF = 1 pulse per

second, which, after a suitable power amplification, drives the transmitting transducer T1. The starting time t_{n1} of the n-th burst is thus known and stored by the controller. The receiver front-end contains a signal amplifier A2 whose gain is automatically controlled by the microprocessor, a time-gating circuit K (killer) and a narrow-band filtering system; this filter is intended to remove the out-of-band noise component affecting the signal and to shape the signal itself. The time-gating circuit connects the amplifier output to the filter only during the time intervals when the sonic pulses are actually received. For this purpose, the gate is enabled at a time t_{kn} related to the time $t_{(n-1)max}$ when the highest relative maximum is detected. We have

$$t_{kn} = t_{(n-1)max} + T - KS \tag{4.1}$$

where T is the pulse repetition period and KS is a suitable constant related to the Q-factor of the filters, the number of their poles and the number of periods of the received signal to be supplied to the band-pass system. In this case, at the end of an iterative process based on the above criteria, the gate is enabled 1 ms before the time of arrival of the signal and disabled 6 ms later. The frequency response of the band-pass filtering system is designed to produce an output signal with a Hamming-type envelope [18]. The output of the filter is then digitized and the time instant associated with the highest relative maximum is identified. This instant is strictly correlated to the arrival time t_{2n} of the received signal. The computation of the TOF can be thus obtained using the relation

$$TOF_n = t_{2n} - t_{1n} \tag{4.2}$$

The system described above allows us to determine the TOF with high accuracy even in the presence of considerable noise, as is usually the case inside the boiler. The method used is also independent of the carrier frequency of the transmitted signal.

5. Experimental results

The performances of the different reconstruction algorithms considered have been first assessed using numerical simulations, in order to carry out a complete quantitative analysis. The TOF data have been numerically evaluated on the basis of a supposedly perfectly known temperature field. We investigated the features of the reconstruction algorithms with respect to the number and positions of the propagation paths, the conditioning of the reconstruction problem and, for the case of the Fourier technique, with respect to the choice of the order of the coefficients to be evaluated and the influence on the solution of the regularization parameter λ. The results of this analysis are reported in [21, 22], and have been used as guidelines for the choice of the reconstruction parameters used here.

The experiments were performed, with both simulated and experimental data, assuming a fixed measurement geometry. The temperature field assumed for the simulation was obtained from a thermal analysis of the boiler; the results of this analysis are very important, in that it is impractical and probably impossible to directly measure the temperature over the entire probed plane. The measurement geometry considered is relative to boiler # 1 of the ENEL power plant located in Santa Gilla, Sardinia, Italy. This boiler has a rectangular cross-section of size 5.929×5.313 m, and it is schematically shown in Figure 4, where the probed plane is also indicated. In Figure 5, the locations of the transmit-

receive devices on the boiler walls are shown together with the assumed propagation paths. As can be noted (see again Figure 4), one of the walls is not accessible and thus does not contain any measurement point.

5.1 Reconstruction from simulated data

In Table I, we report the temperature values resulting from the numerical thermal analysis and adopted for the simulations. These values, distributed on a regular 12 × 13 grid, have been interpolated to obtain the map in Figure 6. On the basis of this map, we calculated the exact TOF data for the paths shown in Figure 5. These data have been used to evaluate the performances of the regularized Fourier technique and of the section-interpolation technique described in *3.2*. The results of the regularization technique with sampling parametrization are not reported here, as they are substantially equivalent to those obtained by the Fourier technique.

In Figure 7 we show an example of Fourier reconstruction. In this case we reconstructed the following Fourier coefficients: A_{00}, A_{01}, A_{10}, A_{02}, A_{11}, A_{20}, A_{03}, A_{30}. The regularization parameter λ has been set to 1. The choice of the above conditions was made assuming the errors in the maximum and mean estimated temperature values and the root-mean-squared error of the reconstructed map as quality indexes for the reconstructions. The percent root-mean-squared error E has been defined by the following expression:

$$E = \frac{\sqrt{\frac{1}{NM}\sum_{j,k=1}^{N,M}\left[T(j,k) - \hat{T}(j,k)\right]^2}}{T_m} \times 100 \qquad (5.1)$$

where NM is the size of the sampling grid and T_m is the true mean temperature. The first two indexes have an evident physical meaning, in that they affect the production of pollutants and the thermal efficiency of the boiler, respectively. In Figure 8, the reconstruction obtained from the same data by the section-interpolation technique is shown. The values found for the quality indexes for the cases in Figures 7 and 8 are shown in Table II. The domain of the reconstruction has been reduced to 4.5 m in the y direction as the reconstructed values are unreliable in the remaining region due to the lack of propagation paths (see again Figure 5). As can be seen, both the reconstruction methods yield good values for the quality indexes. It is also to note that the temperature maps in Figures 7 and 8 are sufficiently close to that in Figure 6, except for the dip in the central region of the boiler, which is just perceivable in Figure 8. This inconvenience is due to the low spatial resolution permitted by the small data set available. Furthermore, in the Fourier case, the contour lines tend to intersect almost orthogonally the boiler walls; this is in contrast with the map shown in Figure 6 a) and also with the thermal behavior of the boiler; this has been found to be a typical drawback of the Fourier reconstruction.

The two techniques considered have also been compared with respect to their robustness against additive noise on the data. For both methods, the mean reconstructed temperature was found to be highly insensitive to noise, with errors less than 10 C for noise standard deviations up to about 0.15 ms. A greater noise-sensitivity was found for the reconstruction of the maximum temperature value, with some advantage for the section-interpolation method; this technique yields excess variations less than 50 C on the maximum temperature for noise standard deviations up to about 0.06 ms.

5.2 Reconstruction from real measurements

The measurement system PYRA, described in Section 4, has been installed in accordance with the geometry shown in Figure 5. The data set which has been considered for our reconstructions is shown in Table III. Each TOF has been corrected for the systematic error related to the sound path inside the horn, between the aperture in the boiler wall and the acoustic transducer. We considered this error to be 0.5 ms. Maintaining the same thermal conditions in the boiler, some temperature measurements have also been made by means of a suction pyrometer placed at different depths in correspondence with apertures # 24, 25 and 26. The results are shown in Table IV.

In Figures 9 and 10, the temperature maps obtained through the Fourier and section-interpolation methods, respectively, are shown. In the case of Figure 9, the number and the orders of the Fourier coefficients and the regularization parameter are those already specified in Section *5.1*. In the case of Figure 10, the same smoothing factor and search radius used in Section *5.1* have been adopted; from available data and physical considerations on the boiler under test, the following temperatures have been imposed at the measurement ports: 1050 °C (port 21), 1070 °C (port 23), 1070 °C (port 24), 970 °C (port 25), 820 °C (port 26), 820 °C (port 27), 1070 °C (port 29). In this case too, the reconstruction domain has been limited as in Figures 6 and 7 and for analogous reasons. In this case, the reliability of the reconstructed values is also questionable in the regions adjacent to the plane y = 4.5 m, where we can observe a physically meaningless increase in the temperature values when approaching the boiler wall.

The two different reconstructions show a fairly good agreement (within a 30 °C range) in the estimated mean and maximum temperatures. A greater difference exists between the minimum values, essentially due to the temperature imposed at ports 26 and 27 in the section-interpolation method. Comparing the shapes of the two contour plots, a substantial agreement can also be observed in the central region of the probed domain, with the exception of the peculiar behavior of the contours in the Fourier reconstruction already observed in Section *5.1*. In Figures 11 and 12, we show the comparison between the temperatures reconstructed by the two methods and the measurements reported in Table IV. Again in this case, we can observe a good agreement between reconstructed and measured values.

6. Conclusions

The measurement of the temperature of the gas inside power plants boilers is an important and not yet completely solved problem. An approach towards its solution is the reconstruction of 2D temperature maps over cross-sectional planes, located in significant positions inside the boiler.

In this paper, we discuss a particular non invasive technique which can be used for this purpose, based on measuring the propagation times of acoustic waves through the considered medium. The architecture of the measuring system consists of transmitter/receiver pairs placed at suitable ports along the walls of the boiler, so that the time-of-flight between the various pairs can be measured. Two techniques for the reconstruction of temperature maps over the entire probed plane have been presented: one is derived from general image reconstruction techniques based on standard

regularization; the other is a procedure that has been designed *ad hoc* for the specific problem.

A comparison of the reconstructed values with the temperature data obtained from a numerical simulation of the thermal process or from direct measurements showed good performances for both of the reconstruction methods described. The quality of our results, and thus the efficiency of our methods, should be evaluated taking into account the following two factors: the extremely small data set available in the case under exam, mainly due to the impossibility of increasing the access ports to the boiler; the fact that the positions of these ports are heavily conditioned by thermal and mechanical constraints. In our opinion, a significant improvement in temperature map reconstruction can only be obtained if greater number of TOF data is available. While this condition can hardly be fulfilled when an acoustic pyrometer system is installed on an already working boiler, as in the case here experimented, far better prospects are possible if the installation of such a measuring system is planned for on the design of the boiler.

7. Acknowledgements

The authors wish to thank Mr. Paolo Stiavetti of the technical staff of IEI-CNR for his programming support.

8. References

[1] S.F. Green, "An Acoustic Technique for Rapid Temperature Distribution Measurements", *J. Acoust. Soc. Am.*, Vol. 77, No. 2, February 1985, pp. 759-763.

[2] S.F. Green, "Acoustic Temperature & Velocity Measurement in Combustion Gases", *Proc. Eighth Int. Heat Transfer Conf.*, San Francisco, USA, 1986.

[3] J.G. Berryman, "Stable Iterative Reconstruction Algorithm for Nonlinear Traveltime Tomography", *Inverse Problems*, Vol. 6, No. 1, February 1990, pp. 21-42.

[4] R.M. Mersereau, A.V. Oppenheim, "Digital Reconstruction of Multidimensional Signals from their Projections", *IEEE Proc.*, Vol. 62, No. 10, Oct. 1974, pp. 1319-1338.

[5] P. Bois, M. LaPorte, M. Lavergne, G. Thomas, "Well-to-Well Seismic Measurements", *Geophysics*, Vol. 37, No. 3, June 1972, pp. 471-480.

[6] S.F. Gull, G.J. Daniell, "Image Reconstruction from Incomplete and Noisy Data", *Nature*, Vol. 272, 20 April 1978, pp. 686-690.

[7] A.N. Tikhonov, V.Y. Arsenin, *Solution of ill-posed problems*, Winston-Wiley, Washington, 1977.

[8] M. Bertero, T.A. Poggio, V. Torre, "Ill-posed Problems in Early Vision", *IEEE Proc.*, Vol. 64, No.8, August 1988, pp. 869-889.

[9] T.A. Poggio, V. Torre, C. Koch, "Computational Vision and Regularization Theory", *Nature*, Vol. 317, 26 September 1985, pp. 314-319.

[10] D.G. Luenberger, *Linear and Nonlinear Programming*, 2nd Ed., Addison-Wesley, 1984.

[11] H.C. Andrews, B.R. Hunt, *Digital Image Restoration*, Prentice-Hall, Englewood Cliffs, NJ, 1977.

[12] E. Salerno, A. Tonazzini: "Image Reconstruction from Line-Integral Data: a Regularization Approach", *Signal Processing V: Theories and Applications*, L. Torres, E. Masgrau and M.A. Lagunas (Editors), Elsevier 1990, pp. 913-916.

[13] E. Salerno, A. Tonazzini, "2D Image Reconstruction from Sparse Line-Integral Data", *Signal Processing*, Vol. 23, No. 2, May 1991, pp. 193-203.

[14] B.D. Ripley, *Spatial Statistics*, John Wiley & Sons, 1981.

[15] D.N. McLain, "Drawing Contours from Arbitrary Data Points", *Computer J.*, Vol. 17, 1974, pp. 318-324.

[16] C.R. Pelto, T.A. Elkins, H.A. Boyd, "Automatic Contouring of Irregularly Spaced Data", *Geophysics*, Vol. 33, 1968, pp. 424-430.

[17] F. Chignoli, A. Gray, "Pirometro Acustico Pyra 100: Misure di Validazione Effettuate sulla Centrale ENEL di Monfalcone. 11-14 giugno 1991", *Bollettino di Analisi e Misure*, CISE-SSE-BM-91.005.

[18] Italian patent No. 91A001, 24/06/1992, extended to USA and EU.

[19] F. Chignoli, "Pyra - Misuratore Acustico di Temperatura di Gas. Installazione e Misure di Validazione presso la Centrale Enel di Livorno, Gruppo 1", *Rapporto di Avanzamento*, CISE-SST-93-7.

[20] F. Chignoli, A. Gray, "Pirometro Acustico Pyra - Misure di Temperatura Effettuate sulla Centrale ENEL di Bastardo", *Bollettino di Analisi e Misure*, CISE-SST-93-18.

[21] ENEL-CNR contract U810/8.65.720.0.252/M03, Reports, September and December 1988.

[22] ENEL-CNR contract U005, Reports, November 1990 and May 1991.

Captions

Figures

1. Schematic cross-section of the boiler with the k-th propagation path.

2. Grid used for uniform sampling of f(x,y) on D.

3. Logic diagram of the PYRA system.

4. Schematic view of the Santa Gilla Boiler #1.

5. Schematic view of the probed plane of the Santa Gilla boiler #1 showing the measurements ports and the propagation paths.

6. a) contour plot and b) surface plot of the data in Table I.

7. a) contour plot and b) surface plot of the reconstructed temperature field by the Fourier technique from simulated data.

8. a) contour plot and b) surface plot of the reconstructed temperature field by the section-interpolation technique from simulated data.

9. a) contour plot and b) surface plot of the reconstructed temperature field by the Fourier technique from real data.

10. a) contour plot and b) surface plot of the reconstructed temperature field by the section-interpolation technique from real data.

11. Comparison between measured and reconstructed temperatures by Fourier technique: a) port #24; b) port #25; c) port #26.

12. Comparison between measured and reconstructed temperatures by section-interpolation technique: a) port #24; b) port #25; c) port #26.

Tables

I. Simulated temperature values (°C)

II. Quality indexes relative to Figures 7 and 8.

III. TOFs measured in the boiler #1 of Santa Gilla plant in accordance with the configuration of Figure 5.

IV. Temperature measurements by suction pyrometer.

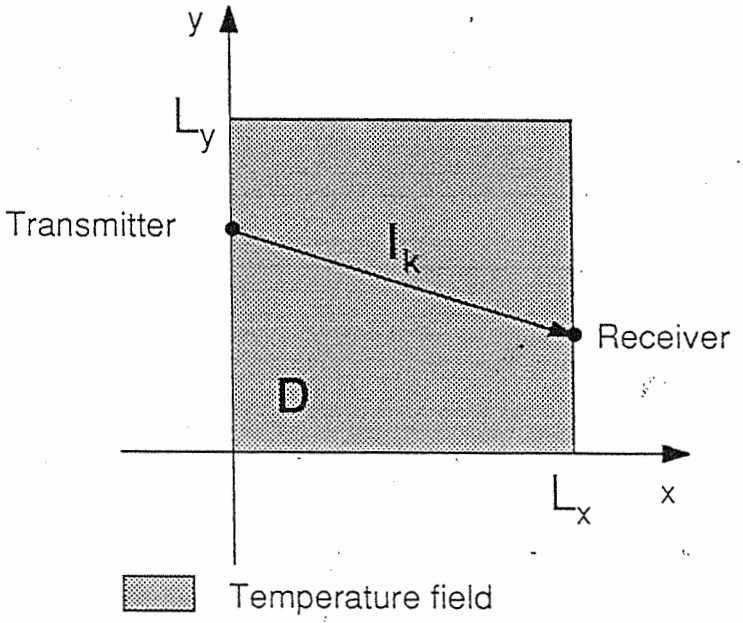

Figure 1

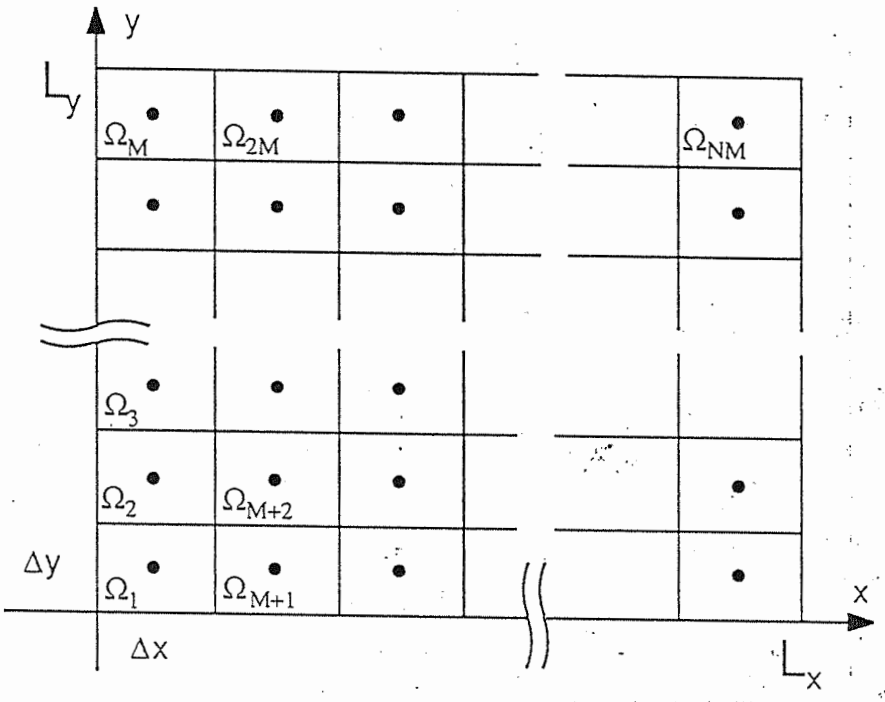
y
L_y
Ω_M
Ω_{2M}
Ω_{NM}
Ω_3
Ω_2
Ω_{M+2}
Δy
Ω_1
Ω_{M+1}
x
Δx
L_x

Figure 2

T1
BOILER
T2
A1
A2
Burst Signal Generator
uP-based Controller
Display/ Store
Gating Circuit (K)
TOF Estimation
Band Pass Filter
Highest relative Maxima detector
A.D.C.

Figure 3

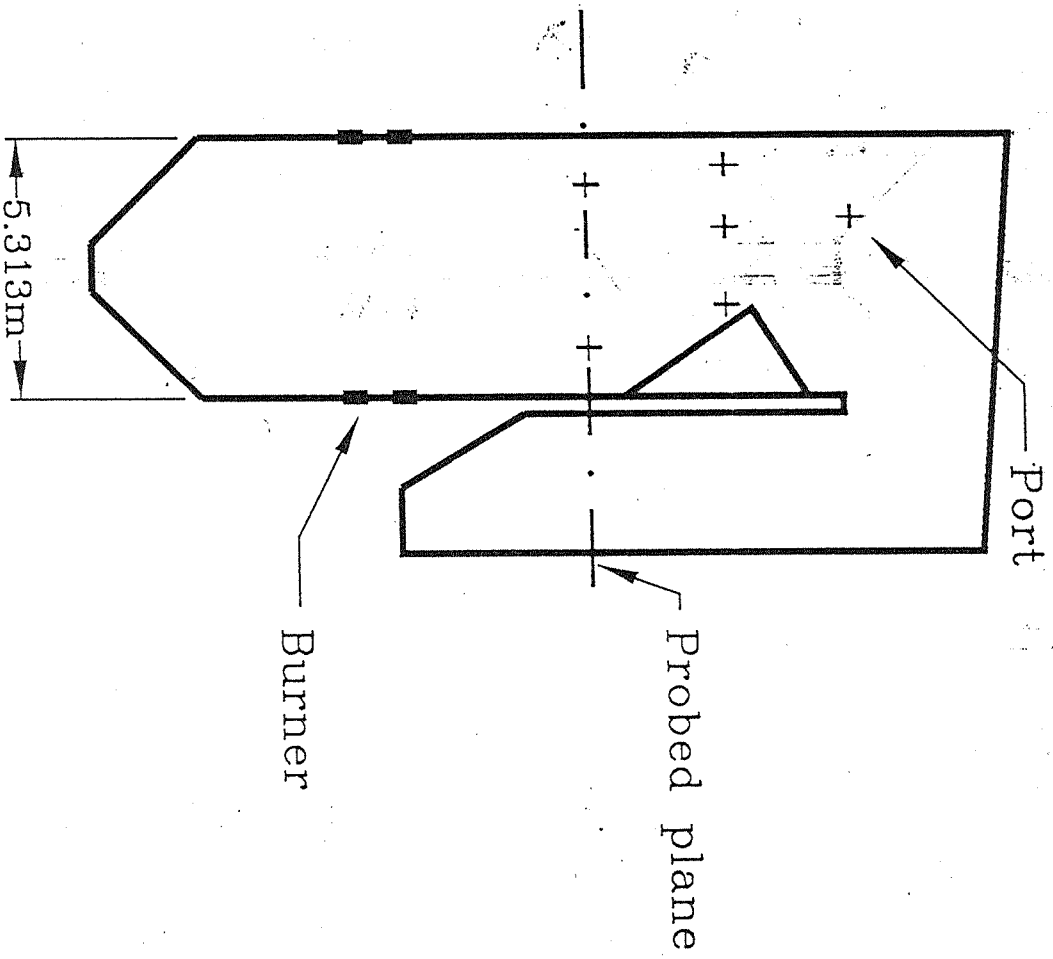

Figure 4

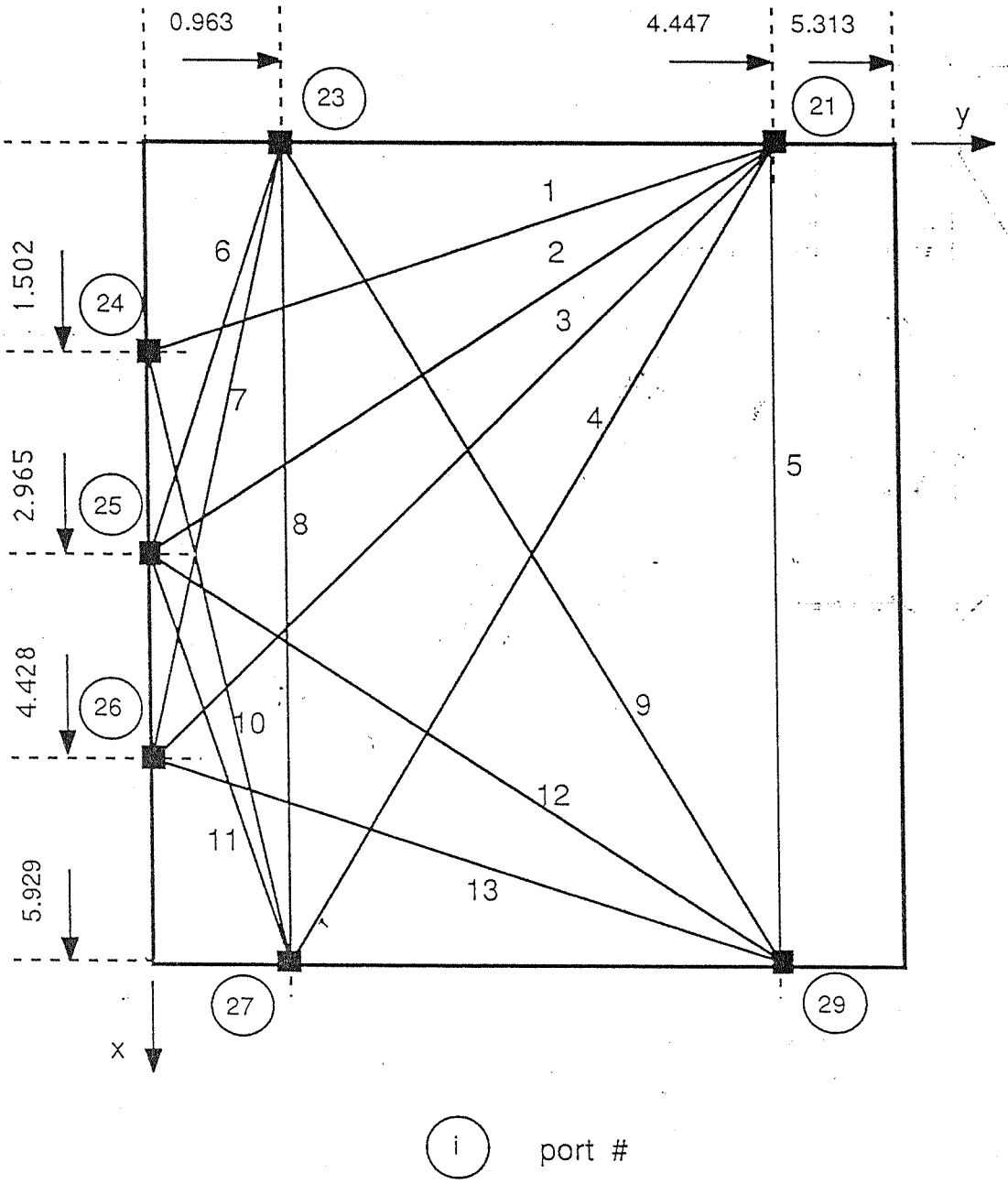
0.963
4.447
5.313
23
21
y
1
2
3
4
5
6
7
8
9
10
11
12
13
1.502
24
2.965
25
4.428
26
5.929
27
29
x
i
port #

Figure 5

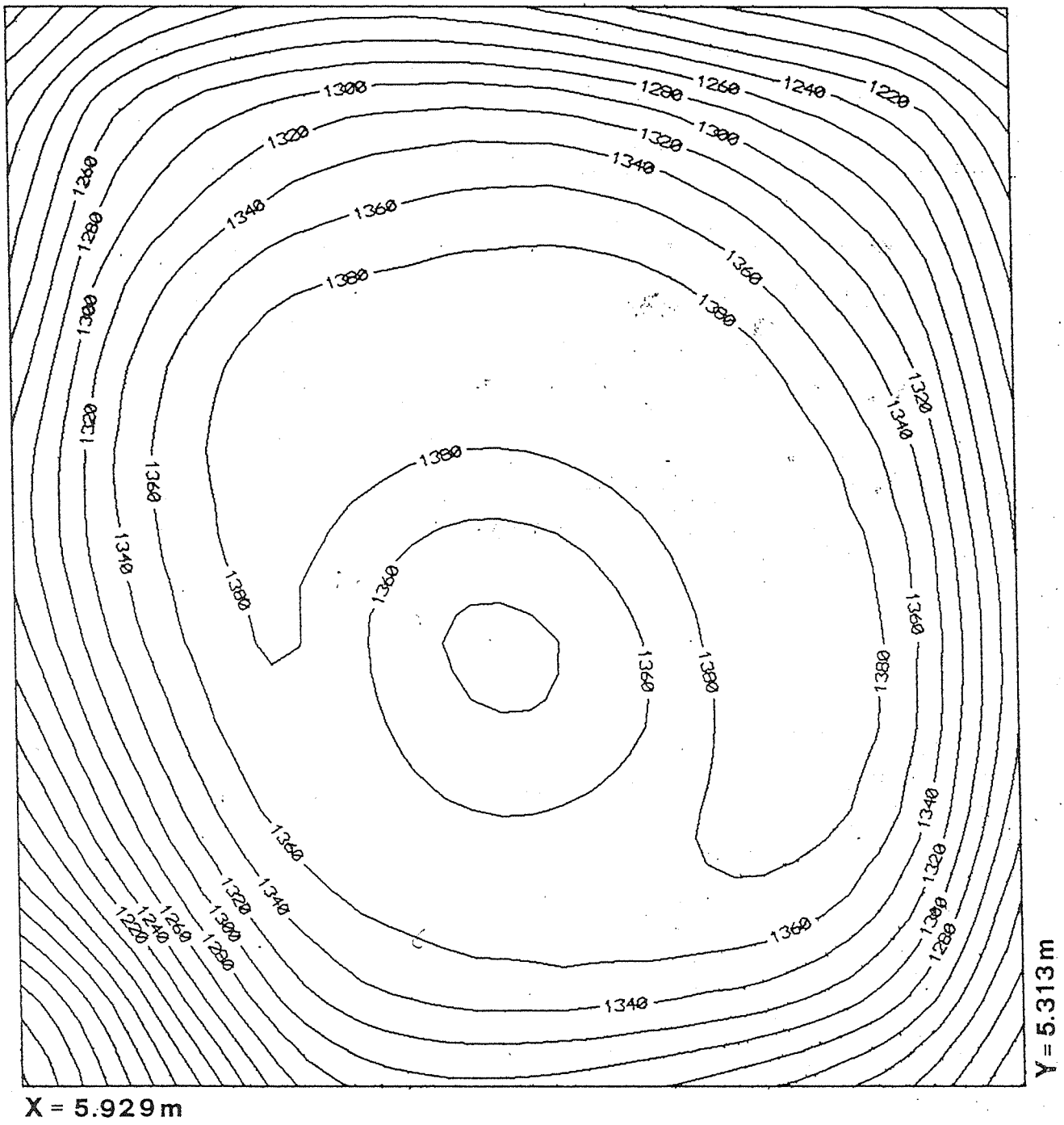

Figure 6 a)

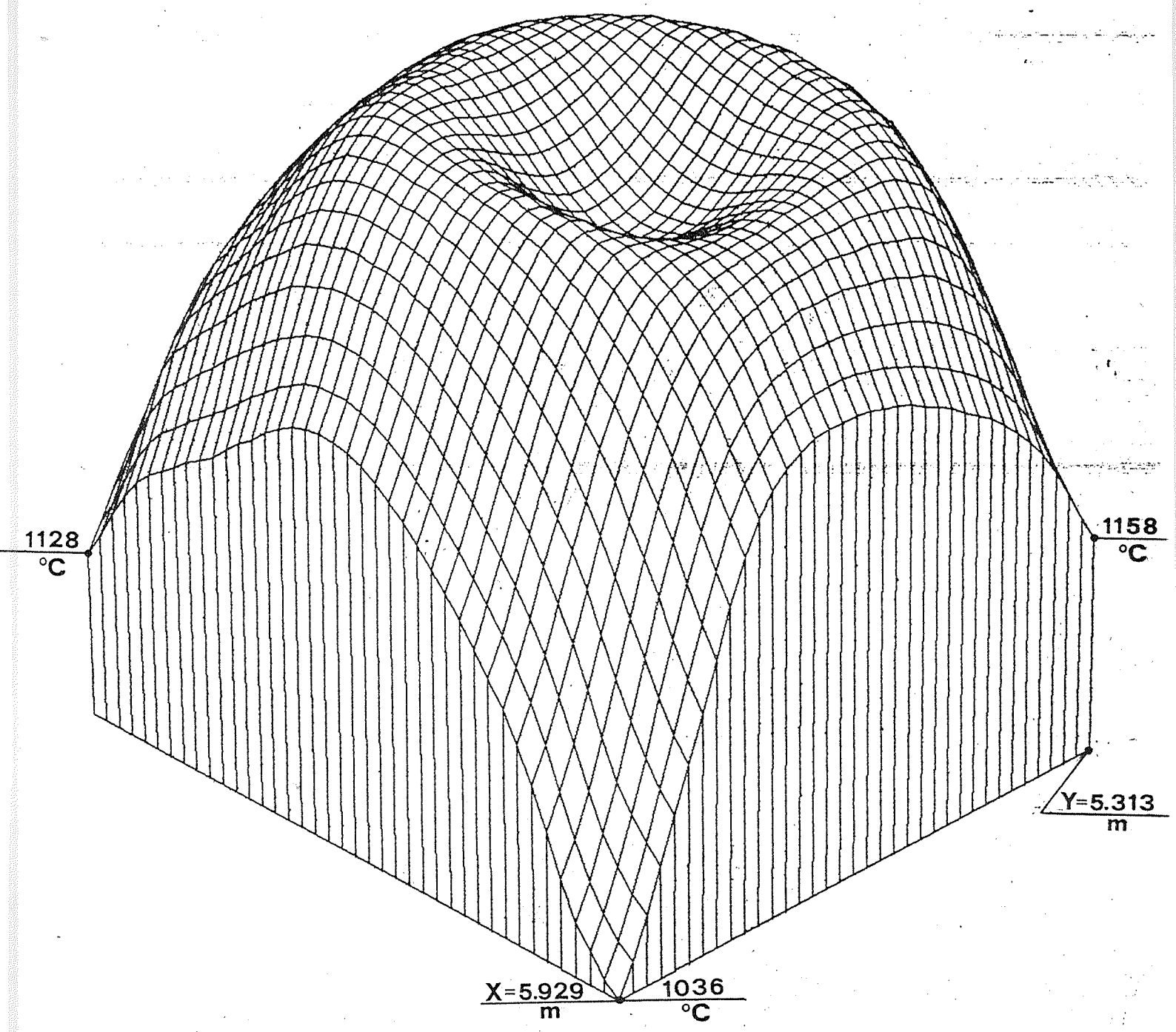

Figure 6 b)

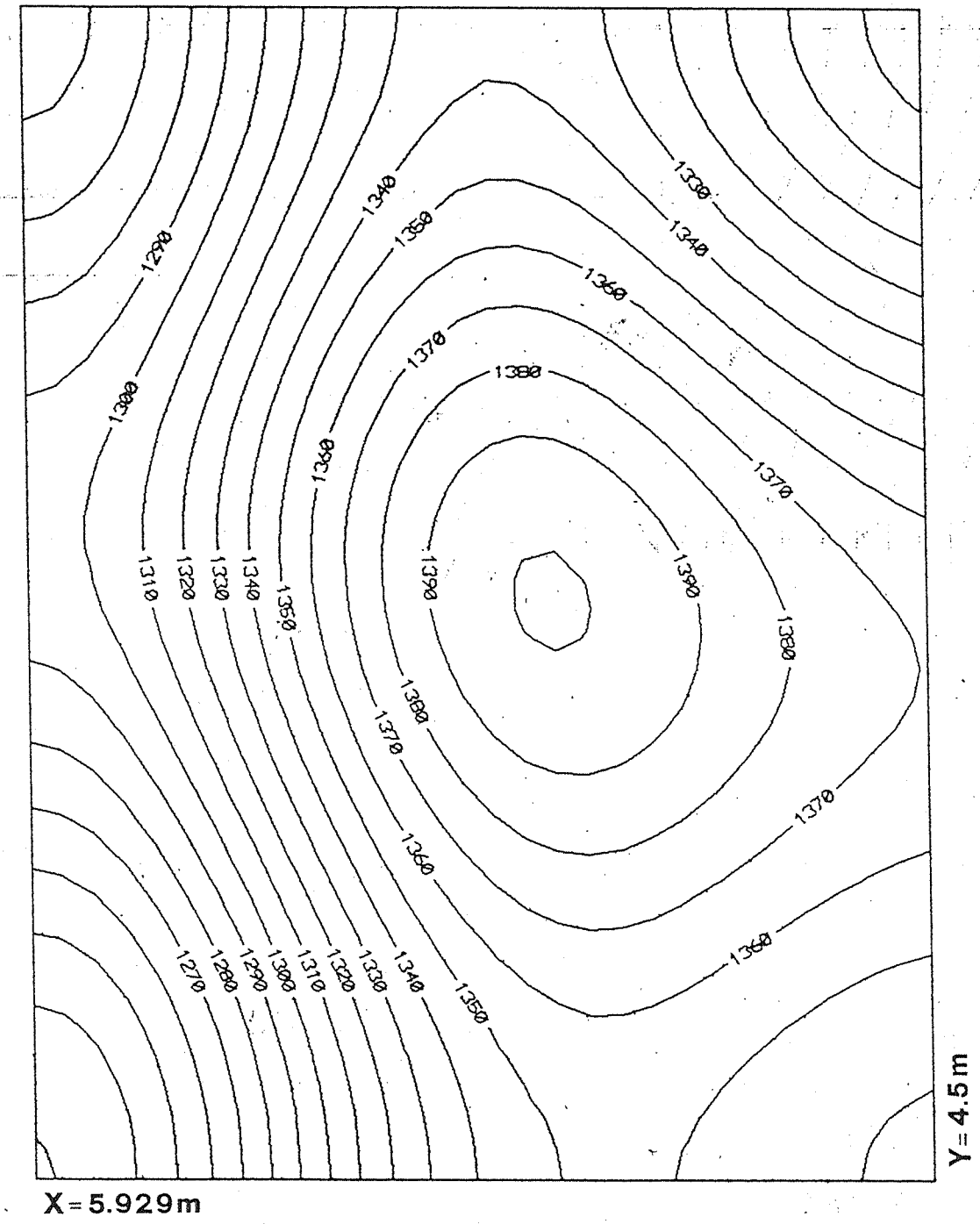
1250
1260
1270
1280
1290
1300
1310
1320
1330
1340
1350
1360
1370
1380
1390
X = 5.929m
Y = 4.5m

Figure 7 a)

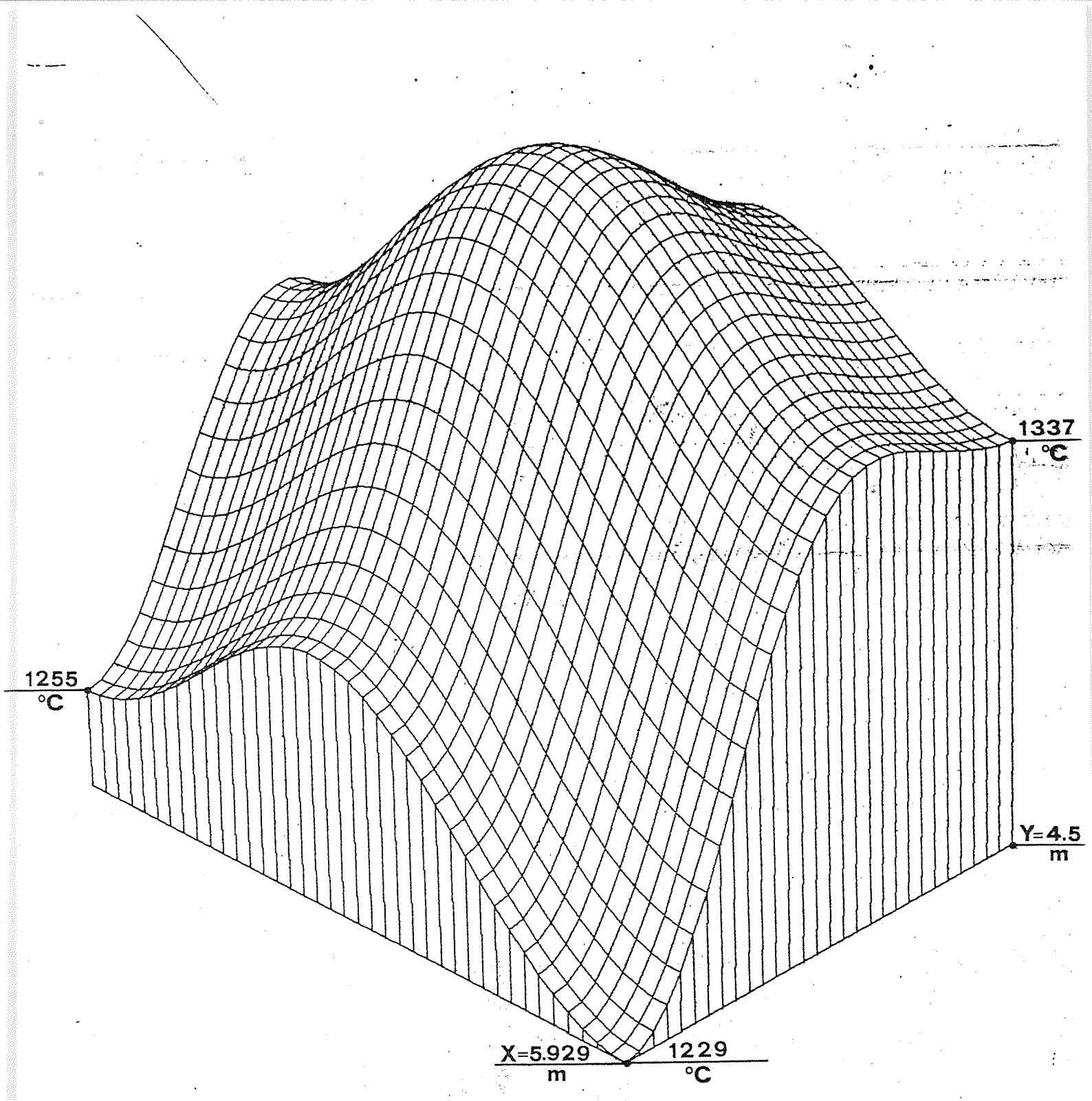

Figure 7 b)

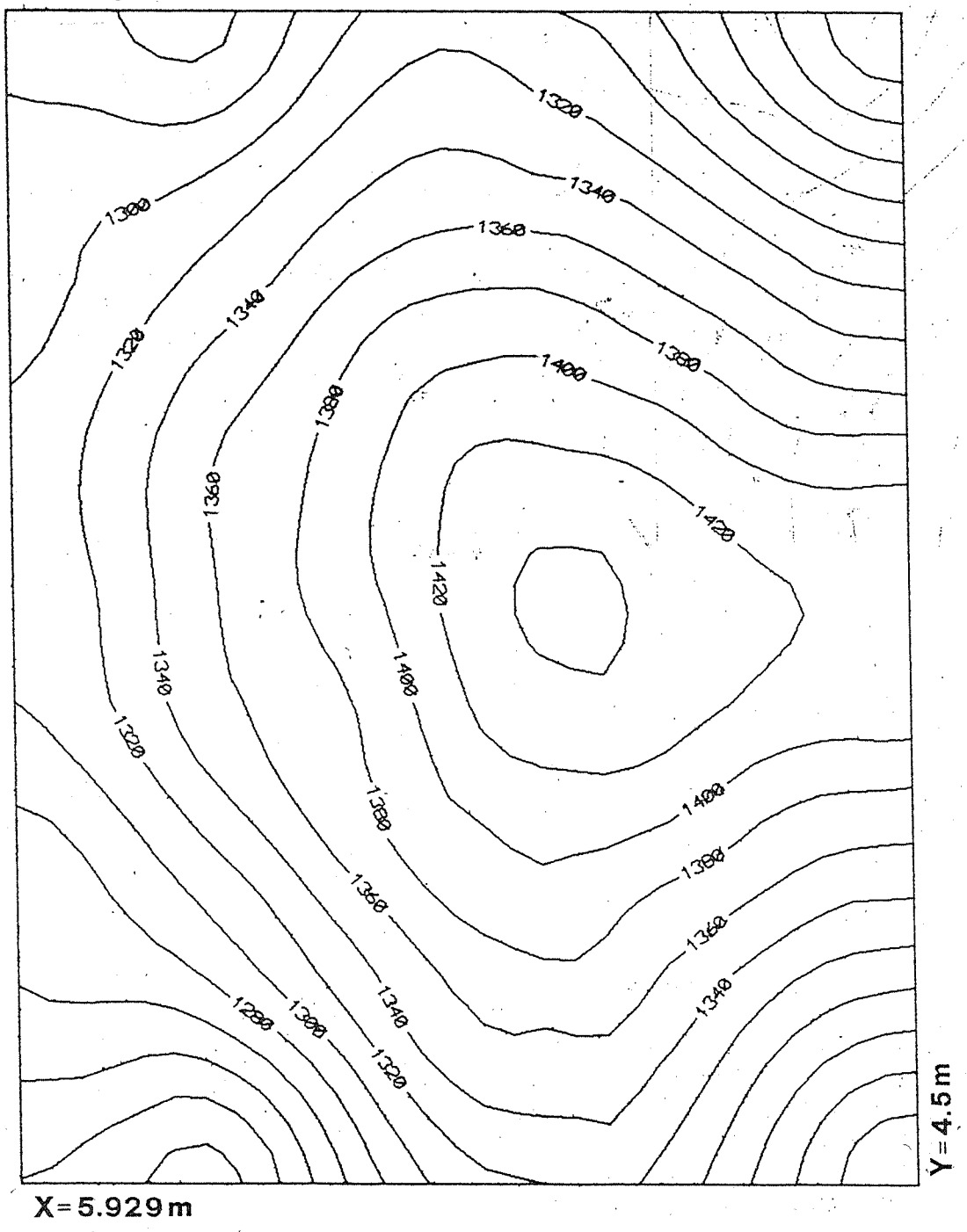

Figure 8 a)

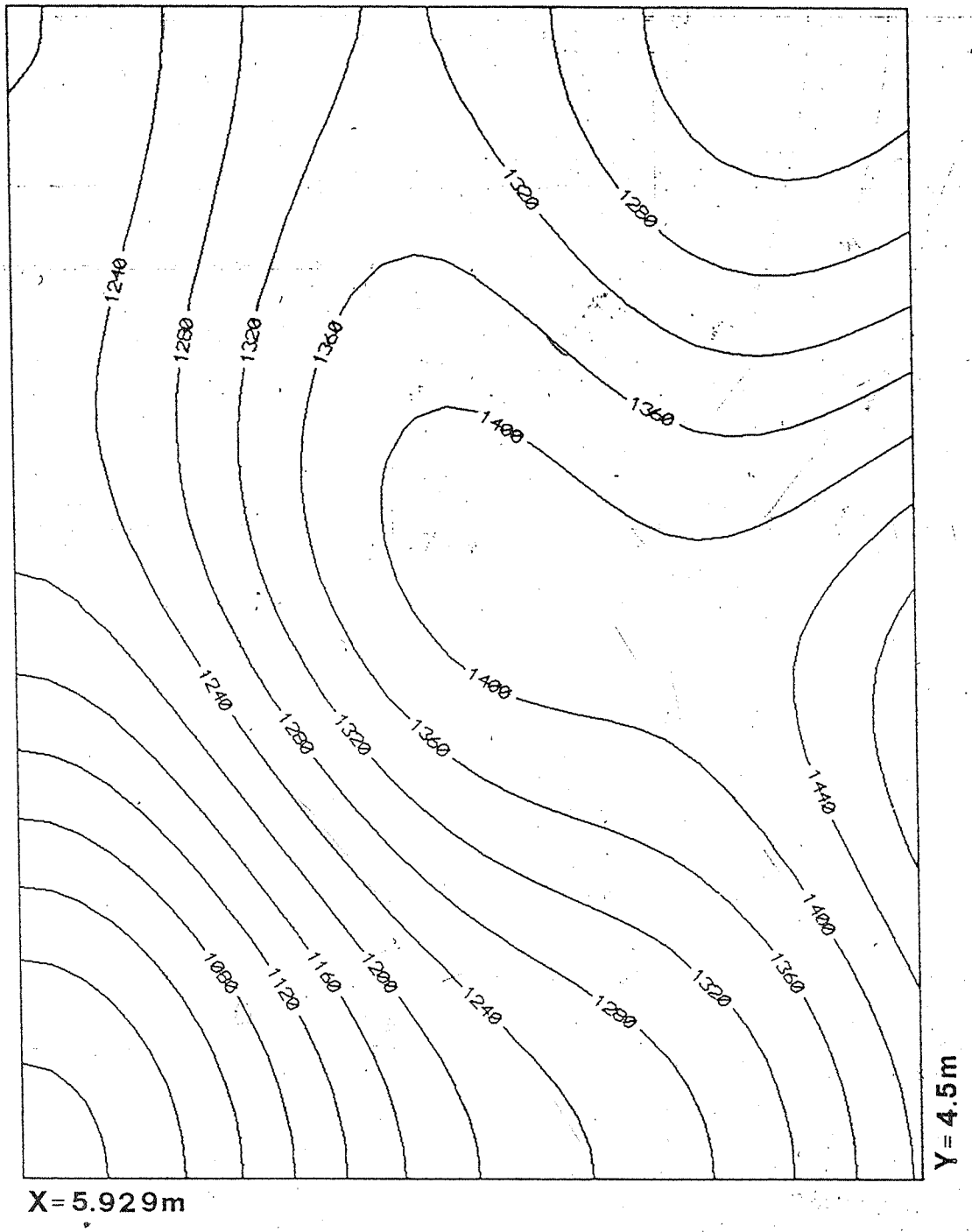
1240
1280
1320
1360
1400
1440
1080
1120
1160
1200
X=5.929m
Y=4.5m

Figure 9 a)

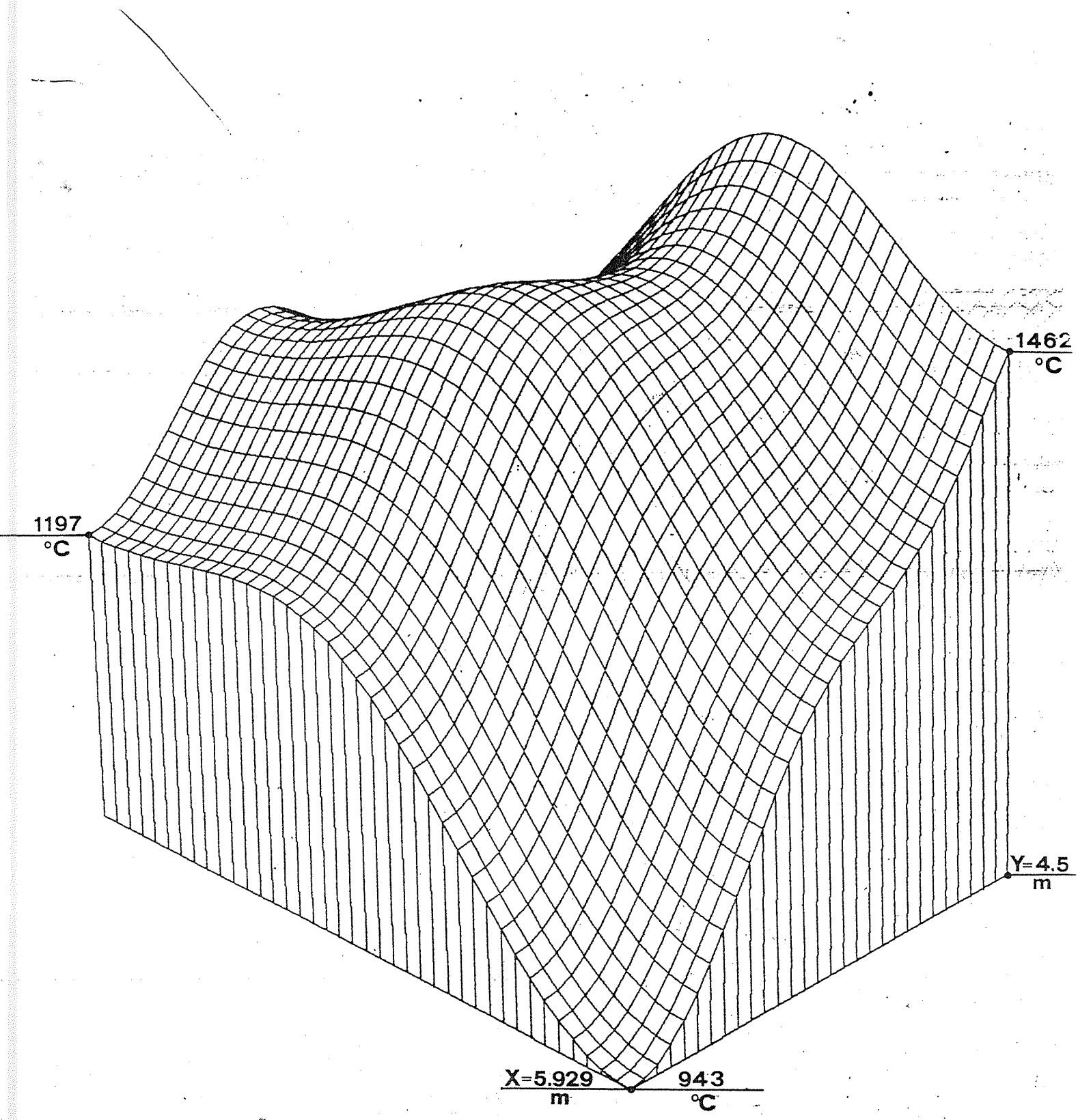

Figure 9 b)

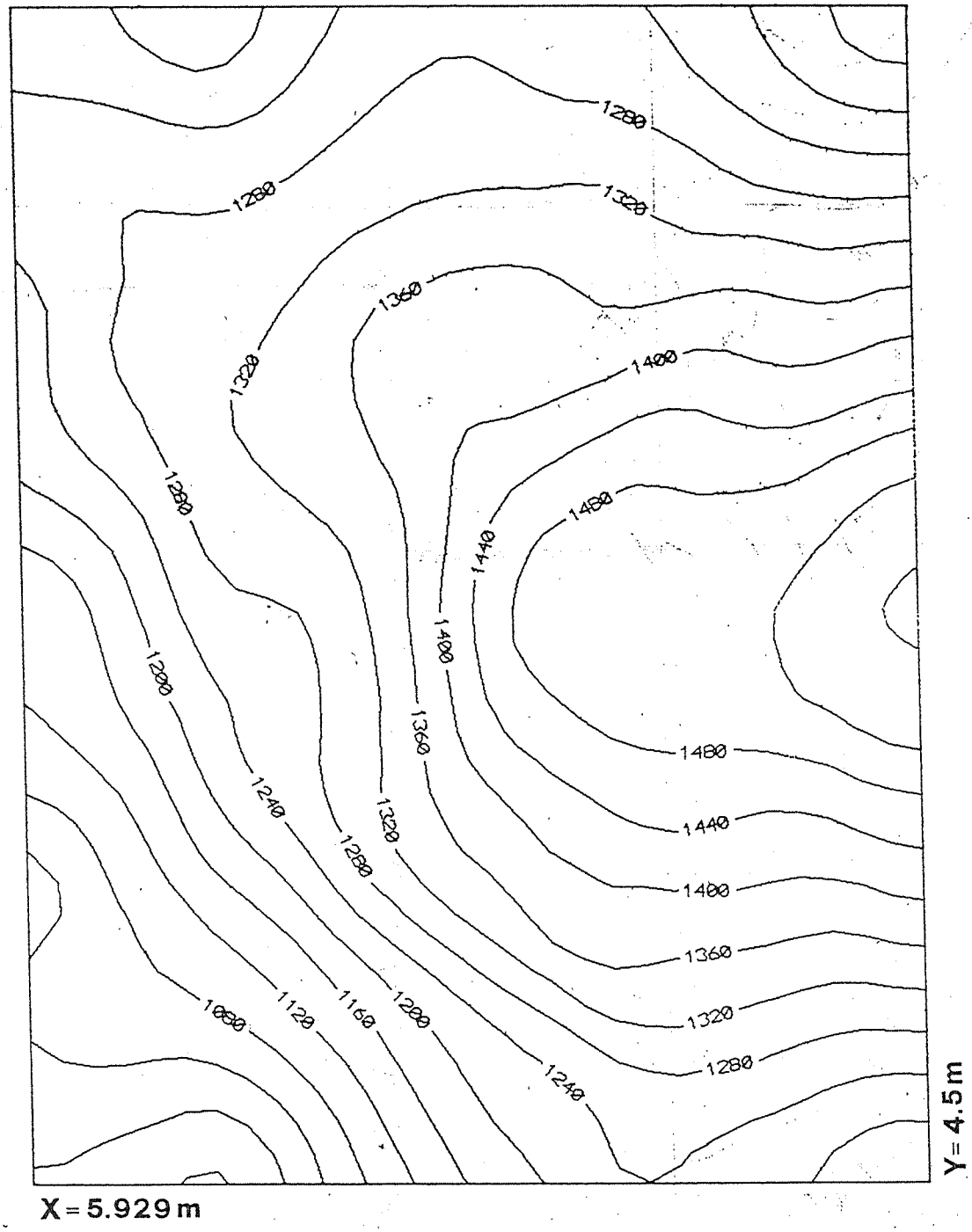
1280
1320
1360
1400
1440
1480
1240
1200
1160
1120
1080
X = 5.929 m
Y = 4.5 m

Figure 10 a)

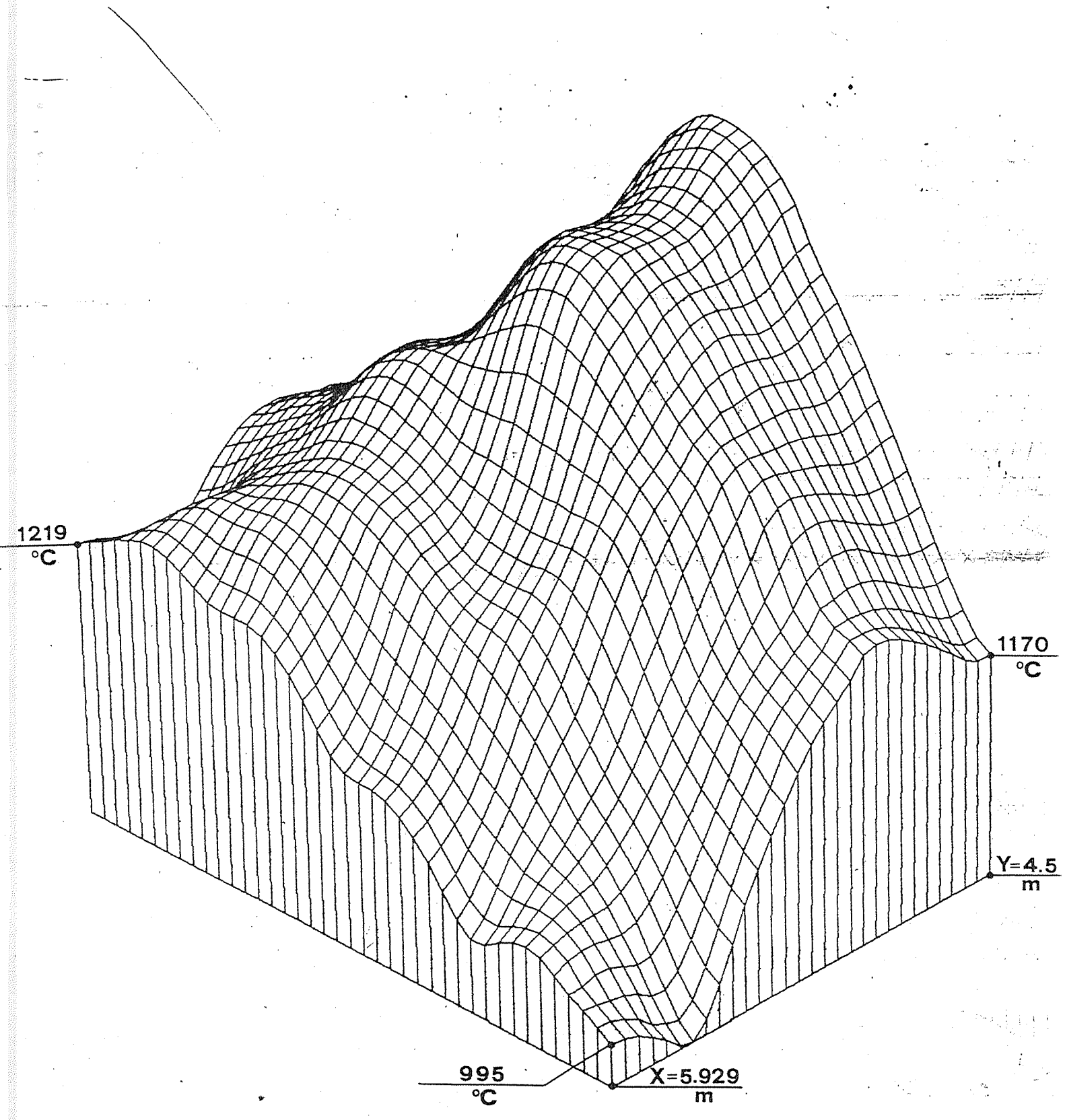

Figure 10 b)

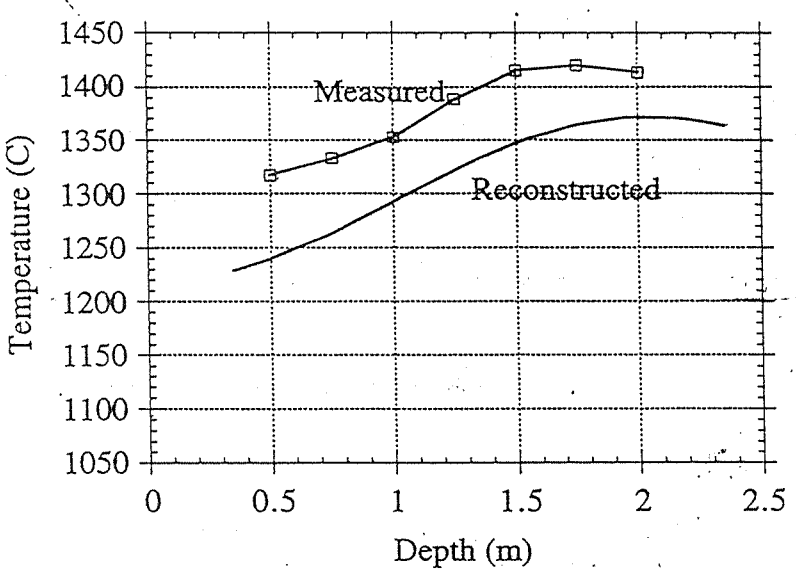

(a)

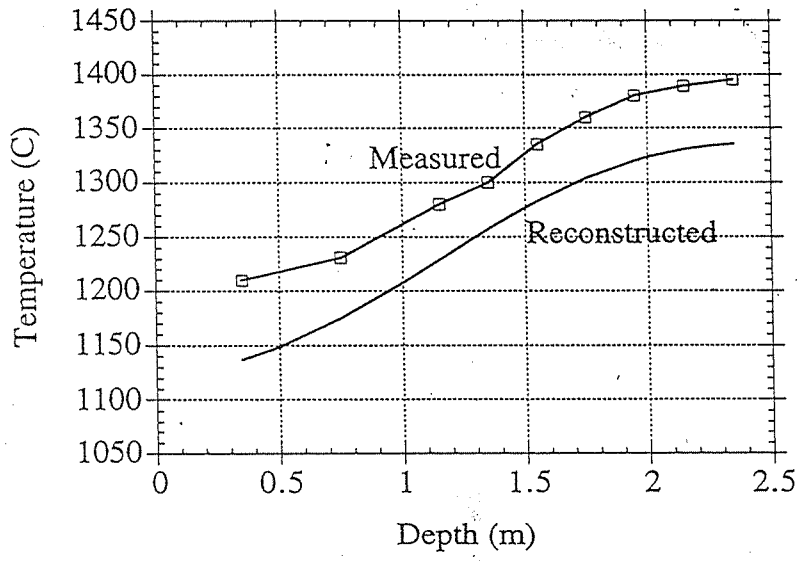

(b)

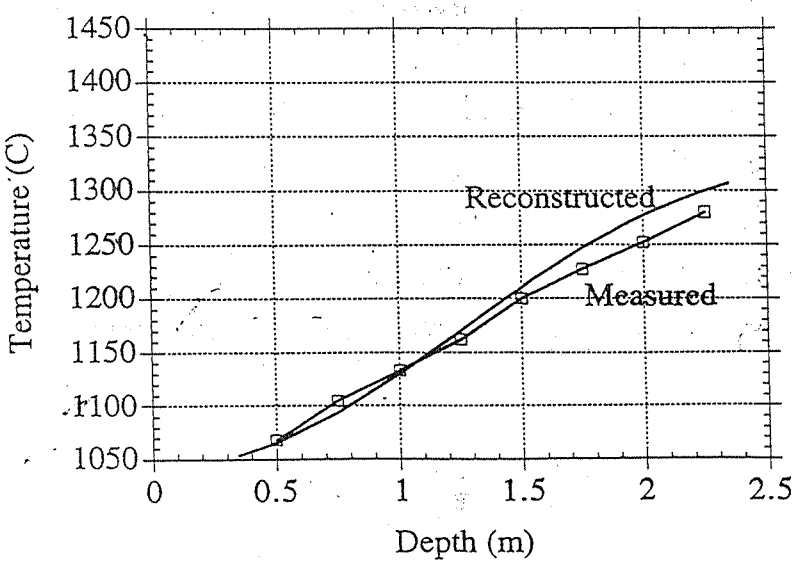

(c)

Figure 11.

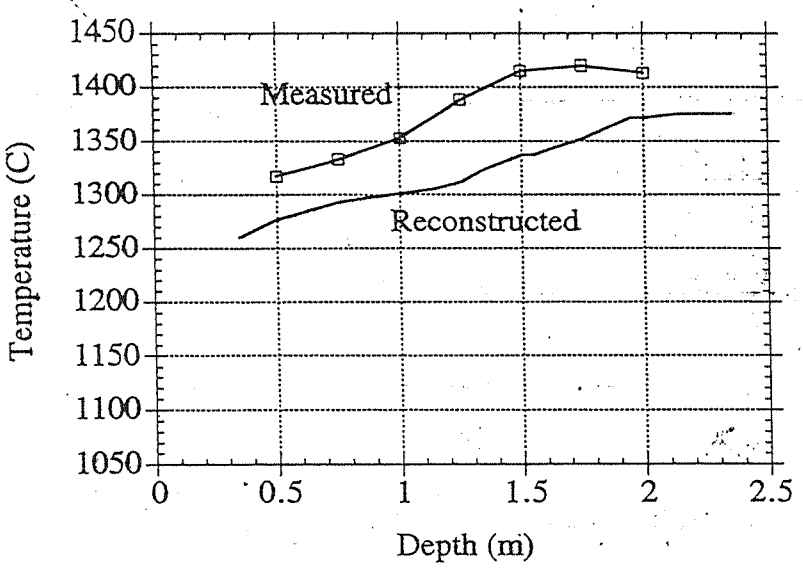

(a)

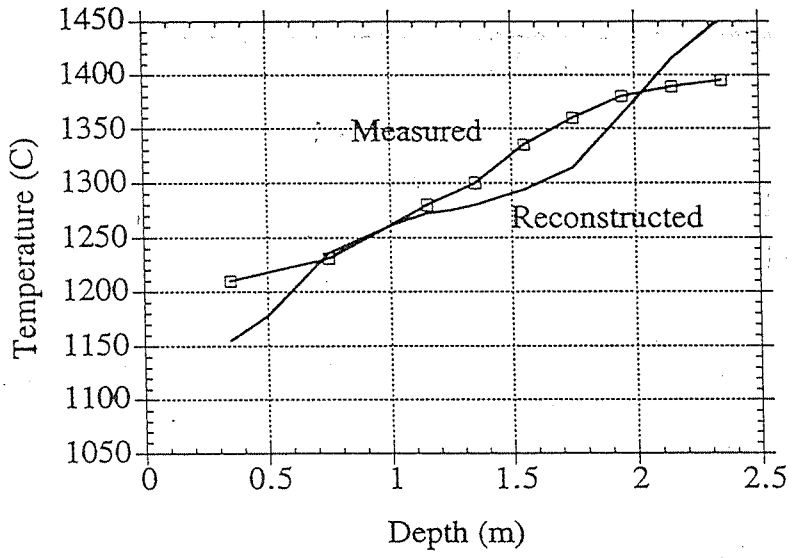

(b)

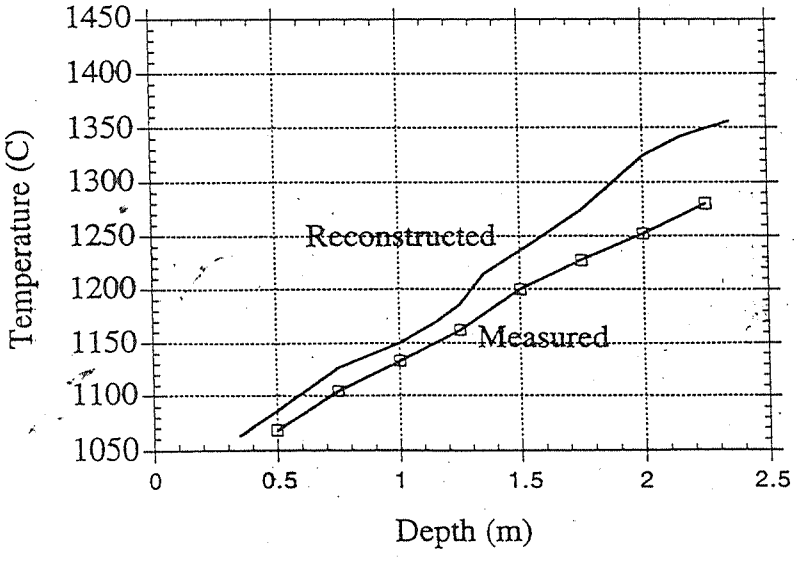

(c)

Figure 12

1123	1176	1199	1217	1241	1262	1264	1249	1222	1187	1142	1066	1031
1176	1246	1275	1305	1325	1335	1332	1319	1294	1262	1215	1142	1103
1204	1283	1313	1347	1371	1377	1375	1366	1352	1330	1294	1242	1179
1222	1302	1339	1375	1395	1393	1386	1384	1381	1369	1348	1312	1260
1228	1312	1352	1381	1398	1386	1365	1355	1362	1369	1364	1341	1288
1224	1316	1359	1387	1397	1377	1350	1332	1342	1361	1368	1350	1294
1211	1311	1361	1388	1395	1381	1355	1339	1341	1362	1372	1351	1289
1191	1296	1353	1384	1396	1391	1375	1362	1360	1373	1375	1346	1278
1173	1270	1330	1368	1391	1400	1400	1393	1388	1387	1376	1337	1262
1161	1245	1296	1332	1361	1381	1393	1396	1392	1384	1362	1315	1241
1145	1218	1261	1291	1316	1337	1352	1359	1357	1343	1313	1268	1209
1110	1165	1194	1214	1230	1243	1255	1260	1257	1241	1213	1187	1155

Table I

	Mean temperature (C)	Maximum temperature (C)	% rms error
Original	1330	1400	-
Fourier	1335	1401	3.21
Section-Interp.	1339	1444	3.16

Table II

Path #	TOF (ms)
1	6.80
2	7.48
3	9.00
4	9.32
5	7.96
6	4.56
7	6.68
8	8.24
9	9.20
10	6.88
11	4.88
12	7.40
13	7.06

Table III

Depth	Temperature (C)		
(cm)	Port #24	Port #25	Port #26
35		1210	
50	1317		1068
75	1333	1231	1105
100	1353		1133
115		1280	
125	1388		1162
135		1300	
150	1415		1200
155		1335	
175	1420	1360	1227
195		1380	
200	1413		1252
215		1389	
225			1280
235		1395	

Table IV